



# Enhanced Oxygen Evolution during Water Electrolysis at De-Alloyed Nickel Thin Film Electrodes

A. Delvaux, Q. Van Overmeere,<sup>a</sup> R. Poulain, and J. Proost<sup>z</sup>

*Institute of Mechanics, Materials and Civil Engineering, Université Catholique de Louvain, B-1348 Louvain-la-Neuve, Belgium*

Hydrogen as an energy carrier has tremendous potential to overcome global warming issues. In this respect, production of hydrogen by water electrolysis has already been intensively studied, but its efficiency, especially in terms of the oxygen evolution reaction (OER), still needs to be improved. The objective of this work is to study the possibility of reducing the OER overpotential by de-alloying Ni thin film electrodes in order to favor bubble detachment. Ni(Al) alloys were first deposited by magnetron co-sputtering, and then chemically leached in a concentrated hydroxide solution with the aim of dissolving out the aluminum. We report X-ray diffraction analysis, scanning electron microscopy, inductively coupled plasma optical emission spectroscopy and roughness measurements to characterize our (de-)alloyed electrodes. Electrochemical testing, both cyclic voltammetry and chrono-potentiometry, has then been realized in a homemade electrochemical flow cell. Results show that different electrode compositions and intermetallic phases can be obtained by varying the deposition parameters, allowing to generate different Al/Ni atomic ratios in the as-deposited films. Moreover, our de-alloyed electrodes present significantly lower overpotentials for the OER than untreated pure Ni electrodes. In the optimal case, a drop of as much as 140 mV was obtained at 10 mA/cm<sup>2</sup>.

© 2017 The Electrochemical Society. [DOI: 10.1149/2.1451712jes] All rights reserved.

Manuscript submitted February 27, 2017; revised manuscript received August 21, 2017. Published September 1, 2017.

Improving the performance of electrodes used in water electrolyzers is one of the multiple requirements to decrease the costs of hydrogen production from renewable electricity. For a constant gas evolution rate at the electrode surface, it is well understood that depending on the rate-limiting step, the overpotential can decrease when the energetics of adsorption of reaction intermediates on the electrode surface is more favorable, or when mass transport of reactants or products are improved. While the former intrinsic electrode kinetics generally depends on electrode composition, atomic structure, and electronic properties of the surface, the detachment of gas bubbles rather depends on the electrode morphology. Inefficient gas bubble detachment from the electrode surface may result in higher overpotentials, both due to a temporary electrical isolation of active sites on the electrode and a decrease in mass transport effectiveness at the electrode surface.<sup>1,2</sup> Moreover, the pressure exerted by gas bubbles may also degrade the electrode mechanically.<sup>3</sup> In this respect, tuning the detachment of gas bubbles through morphological engineering of DSA-type electrodes has already been demonstrated to be highly beneficial for both the chlorine<sup>1,2</sup> and the oxygen evolution reaction.<sup>4</sup> However, when different electrode morphologies are compared, it is not always straightforward to attribute a lowering of the overpotential to either an increase in surface area or to an improved bubble detachment.<sup>4,5</sup> This is particularly true for thick electrodes, where there can be a marked difference between the inner electrode structure and the outer electrode surface behavior. In this contribution, we therefore use morphologically controlled nickel thin film electrodes, obtained by de-alloying Ni(Al) thin films, to provide a systematic understanding of the factors that improve bubble detachment from electrode surfaces. Nickel is a primary candidate material for the OER due to its low cost, relative abundance, its high electrochemical activity and its long-term stability in alkaline conditions.<sup>6</sup>

## Experimental

**Electrode synthesis.**—Ni(Al) alloy films of various compositions were deposited with a thickness of about 50 nm by magnetron co-sputtering from separate Ni and Al cathodes (Kurt J. Lester Co.) in a multi-target sputtering chamber (Orion 5 from AJA International). Deposition power and time were modified independently on each target in order to obtain different initial Al/Ni atomic ratios of 0, 0.2, 0.4 and 0.7 respectively. These can then also be expected, according to the theoretical Al-Ni phase diagram taken from Ref. 7 and shown in Figure 1a, to lead to different intermetallic phases: pure Ni, a mix of

Ni and AlNi<sub>3</sub>, a mix of AlNi<sub>3</sub> and the metastable phase Al<sub>3</sub>Ni<sub>5</sub>, and AlNi, respectively. Prior to deposition, Si substrates were cleaned in a H<sub>2</sub>SO<sub>4</sub>/H<sub>2</sub>O<sub>2</sub> bath (5:2 in volume) at 80°C during 10 min, dipped in 2% HF during 20 s to etch its native oxide, and rinsed in H<sub>2</sub>O during 10 min. Prior to the Ni(Al) layer, the Si substrates were first passivated by a 4 nm TiO<sub>2</sub> layer, deposited by RF magnetron sputtering from a TiO<sub>2</sub> target without breaking the vacuum. The ultrathin TiO<sub>2</sub> layer is corrosion resistant while still allowing electron transfer by tunneling between the silicon and the nickel electrode. The base pressure prior to deposition of TiO<sub>2</sub> was lower than 3·10<sup>-7</sup> Torr, while deposition itself was performed at 2 mTorr in an Ar atmosphere. Purity levels of the TiO<sub>2</sub>, Al and Ni targets were 99.99%, 99.9995% and 99.995%, respectively. Al was then selectively leached in an ultra-pure stagnant 30 wt% KOH solution made from KOH pellets (≤0.001% trace metals, Sigma-Aldrich) at room temperature to produce de-alloyed Ni electrodes.

**Microstructural characterization.**—The microstructure of the electrodes was observed with Scanning Electron Microscopy (SEM, ZEISS Ultra-55) using its secondary electron detector. A Bruker D8 Advance was used to determine the phase composition of the thin films by X-ray diffraction (XRD). For these measurements, a Co-K<sub>α</sub> X-ray source was directed at 30 kV and 30 mA toward the sample at an angle of 2° with respect to the sample surface. The 2θ angle was varied from 20° to 100° in steps of 0.02°, and a Braun linear position sensitive detector was used to collect the photons.

The stoichiometry of the films was evaluated by dissolving them into acid solutions, which were then analyzed by inductively coupled plasma optical emission spectrometry (Agilent Technologies 5100 ICP-OES). An alumina torch was employed for the measurement due to its higher resistance to concentrated KOH. The detection limit for Ni and Al was on the order of 0.01 ppm. Once the quantity of each element was determined, these values were then normalized by the total area of the sample which has been dissolved.

Finally, atomic force microscopy (AFM, Bruker Multimode Nanoscope V) was used to characterize the electrode morphology and to obtain roughness measurements. AFM was employed in tapping mode, using a silicon cantilever (PPP-NCHR, PointProbe Plus Non Contact – High Resonance Frequency – Reflex Coating) with a pyramidal-shaped tip. This cantilever had an Al coating on the detector side, was made of highly doped silicon in order to dissipate static charge, and has a spring constant of 42 N/m. Its typical tip radius is less than 7 nm and its resonance frequency is 330 kHz. For each sample, two regions were analyzed at three different length scales (1, 9 and 100 μm<sup>2</sup>). From these topological data, RMS values were

<sup>a</sup>Present address: Palo Alto Research Center, Palo Alto, California 94304, USA.

<sup>z</sup>E-mail: joris.proost@uclouvain.be

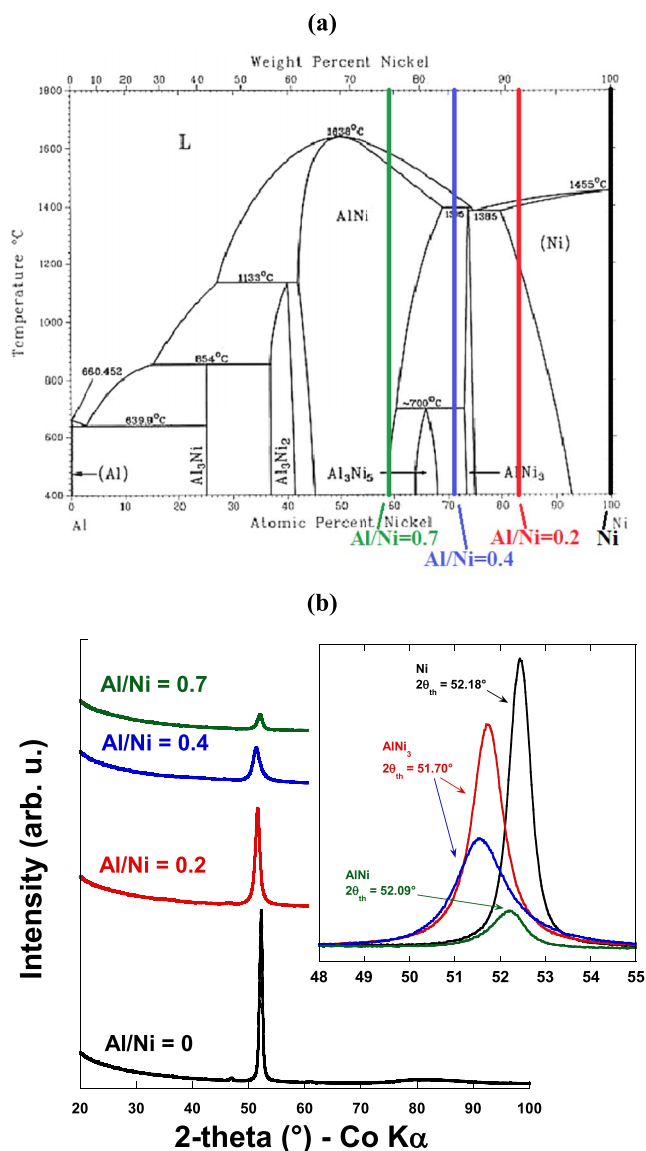


**Figure 1.** (a) Theoretical Ni-Al phase diagram as taken from Ref. 7 with an indication of the compositional range covered in this work by the different alloyed Ni(Al) films (note that at%Ni =  $100/(1+\text{Al}/\text{Ni})$ ); (b) measured X-ray diffractograms for different Al/Ni ratios after sputter deposition. Together with the magnified diffractograms, the theoretical  $2\theta$  angles for the most intensely diffracting planes of each of the expected Ni-Al phases (including pure Ni) has been included as well.

then extracted using Gwyddion software and averaged for each length scale.

**Electrochemical measurements.**—A home-made 25 mL PTFE electrochemical cell in a flowthrough configuration was used. PTFE decreases possible electrode contaminations resulting from glass etching in alkaline solutions. The cell was systematically cleaned in dilute aqua regia and rinsed with copious amounts of water between experiments to avoid trace metal contaminations. The geometric area of the electrode exposed to the electrolyte was measured to be 1.131 cm<sup>2</sup>. The working electrode was upward-facing to avoid bubble accumulation on its surface.<sup>3</sup> The electrolyte flowrate was controlled by a peristaltic pump. Tygon tubing (Chemical Grade) was connected to the electrode flow channels. An ohmic contact with the silicon substrate was made by scratching an InGa eutectic.

The electrolyte was a 1.0 mol/L KOH solution ( $\leq 0.001\%$  trace metals, Sigma-Aldrich), kept at room temperature. Because of their

well-known influence on the OER kinetics,<sup>8</sup> the level of Fe impurities in the electrolyte was measured by ICP-OES to be on the order of 1.7 ppm. Millipore water (18.2 M $\Omega$  cm) was used to prepare the KOH solutions, rinse the cell and the electrodes. The equilibrium potential was set at 1.23 V vs. the Reversible Hydrogen Electrode (RHE) by sparging the electrolyte with 99.9999% pure O<sub>2</sub> (Praxair). Oxygen was sparged during 15 min before the experiments to ensure electrolyte saturation. The counter and reference electrodes were, respectively, glassy carbon (HTW Hochtemperatur-Werkstoffe GmbH) and Ag/AgCl/KCl<sub>sat</sub> (Radiometer Analytical). All potential differences reported herein are referenced to the RHE:

$$E_{RHE} = E_{Ag/AgCl} + E_{T,corr} + 0.059 \text{ pH} \quad [1]$$

where  $E_{Ag/AgCl}$  is the measured potential and  $E_{T,corr}$  is the temperature correction factor for the Ag/AgCl/KCl<sub>sat</sub> reference electrode, equal to 0.204 V at 20°C. A Metrohm Autolab PGSTAT302N potentiostat with FRA 32M impedance and SCAN250 modules was used for the electrochemical experiments. Cyclic voltammetry (CV) at 10 mV/s during 8 cycles and chrono-potentiometry at 10 mA/cm<sup>2</sup> during a few hours were used to determine electrode performance and stability. Potentials were also corrected for the uncompensated resistance ( $R_u$ ) of the electrolyte, for which a  $R_u$  value of 7  $\Omega$  was measured by positive feedback and Electrochemical Impedance Spectroscopy (EIS). Moreover, CV data were corrected for capacitive effects by averaging forward and backward cycles.

## Results and Discussion

**Electrode composition and morphology.**—XRD was used to obtain diffractograms of our Ni(Al) thin films for the different Al/Ni atomic ratios, both after sputter deposition, after Al leaching, and after electrochemical cycling. Results shown in Figure 1b indicate that already after sputter deposition, the intensity and the position of the peaks are different for all samples. The one for the pure Ni film (52.45° for Al/Ni = 0) can be assigned to the pure face-centered cubic Ni phase. The peak of the Al/Ni = 0.2 film (51.72°) corresponds to the AlNi<sub>3</sub> phase, which also fits with the peak of the Al/Ni = 0.4 film (51.55°). However, with the additional information that one of the theoretical diffraction peaks for the Al<sub>3</sub>Ni<sub>5</sub> phase is expected at 51.30°, it is very reasonable to assume that the Al/Ni = 0.4 electrode is rather a mix of both AlNi<sub>3</sub> and Al<sub>3</sub>Ni<sub>5</sub> phases. Finally the AlNi phase can be assigned to the peak on the Al/Ni = 0.7 sample (52.20°). All these results are in direct agreement with the Ni-Al phase diagram shown in Figure 1a.

After the Al leaching step the same phase composition is still present, indicating that only a small fraction of Al has passed into solution. Nevertheless, the mean peaks on the diffractograms are slightly shifted to the left for the electrodes with Al/Ni ratios equal to 0.2, 0.4 and 0.7. This shift corresponds to  $-0.27\%$ ,  $-0.29\%$  and  $-0.36\%$ , respectively. The peak position is also shifted after electrochemical cycling:  $-0.38\%$  for the pure Ni electrode,  $+0.11\%$  for the Al/Ni = 0.2 electrode and  $+0.15\%$  for the Al/Ni = 0.7 electrode. However, the position of the peak did not change for the Al/Ni = 0.4 electrode.

ICP was used to analyze the film composition before and after Al leaching. Table I shows that the Al/Ni ratio is only slightly changed by the leaching step, meaning that chemical dissolution is not very selective. This result confirms the XRD analysis that no phase changes occurred before and after the leaching step. Nevertheless, as shown in Figure 2, Al and Ni are individually still being leached out of the

**Table I.** Al/Ni ratio obtained from ICP-OES analysis before and after leaching.

| Al/Ni before leaching | Al/Ni after leaching |
|-----------------------|----------------------|
| $0.23 \pm 0.01$       | $0.21 \pm 0.01$      |
| $0.42 \pm 0.03$       | $0.40 \pm 0.03$      |
| $0.74 \pm 0.04$       | $0.71 \pm 0.04$      |

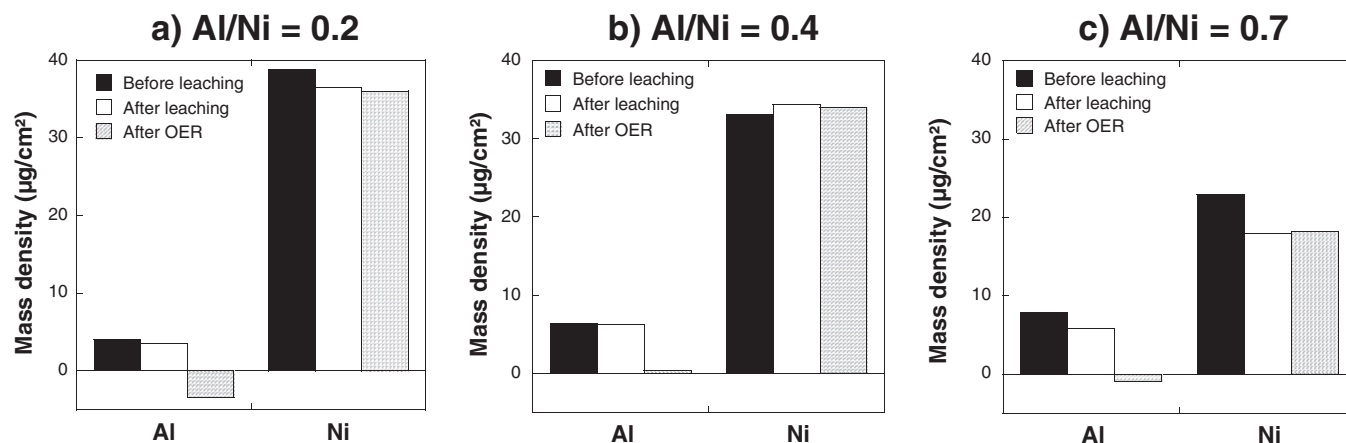


**Figure 2.** Al and Ni mass densities before leaching, after leaching, and after electrochemical cycling, for electrodes with initial Al/Ni ratio of a) 0.2, b) 0.4 and c) 0.7. Note that the apparent negative Al mass densities calculated for the 0.2 and 0.7 films results from statistical error propagation when subtracting the Al base-line signal from the acids used for complete dissolution of the films before ICP-OES analysis.

thin film, thereby still modifying the electrode surface morphology. This is especially pronounced after electrochemical cycling in a 1 M KOH electrolyte, when almost all of the Al is being leached out. Note that from the same figure, no additional Ni was found by ICP-OES, within the analytical error margins, to leach out during electrochemical cycling. From these graphs, it also turns out that the Al/Ni = 0.7 thin film (c), constituted of the AlNi phase, is the most soluble one, and the Al/Ni = 0.4 electrode (b), containing a mixture of AlNi<sub>3</sub> and Al<sub>3</sub>Ni<sub>5</sub>, the least soluble one.

Regarding the relative solubilities of the different Al-Ni phases, recent results from Moller et al.<sup>14</sup> indicated that the standard Gibbs free energy  $\Delta G^\circ$  for the chemical alkaline leaching of Al from Al/Ni intermetallics generally increases (in absolute value) with increasing Ni content. This would then result in the following increasing solubility order (values of  $\Delta G^\circ$  taken from Ref. 14 are given between brackets): Al<sub>3</sub>Ni (-1157.3 kJ) > Al<sub>3</sub>Ni<sub>2</sub> (-1026.7 kJ) > AlNi (-318.4 kJ) > AlNi<sub>3</sub> (-284.4 kJ). Although no thermodynamic values were given for the metastable Al<sub>3</sub>Ni<sub>5</sub> phase, one would expect it to be somewhat more soluble than the AlNi phase as well, based on its higher Ni content. As a result, we would at first sight expect the Al/Ni = 0.4 electrode to be the most soluble one, rather than the Al/Ni = 0.7 film. However, it should be noted that, when plotting the above  $\Delta G^\circ$  values as a function of Al/Ni ratio, a sharp decrease in solubility can be seen for Al/Ni ratio's < 1, after which values rather seem to plateau out. Therefore, the difference in solubility (based on the cited  $\Delta G^\circ$  values) would not be that significant after all. Moreover, we should also remind that most of the roughening and solubility effects that we observed occurred after electrochemical cycling, related to additional leaching out of Al into the electrolyte. The latter is obviously electrochemical in nature, for which the results with respect to chemical leaching of Ref. 14 might not be the appropriate reference point.

Finally, from the AFM measurements on the electrode surface, one can observe in Figure 3 that the RMS roughness of our de-alloyed electrodes after leaching (but before electrochemical cycling) is not significantly higher than the roughness of the pure Ni electrode. However, after cyclic voltammetry, the roughness of the pure Ni electrode stays constant, while the one of the de-alloyed electrodes increases significantly: an RMS increases of a factor 5.6, 2.2 and 3.5 being measured for the Al/Ni = 0.2, 0.4 and 0.7 thin film electrodes, respectively. This can be attributed to the fact that most of the additional Al is being leached out during the OER, as already evidenced in Figure 2. It is also fully in line with the theoretical Pourbaix diagram for the Al/Ni system presented in Ref. 14 which indicates that in our pH and potential operating range, no Al<sub>x</sub>Ni<sub>y</sub> phases are stable. As a result, all of the Al should leach out of the electrode, and only hydrous Ni species are predicted to be stable under OER conditions at pH = 14.

#### *Influence of electrode composition and morphology on the OER performance.*

—To compare the OER behavior of our different de-alloyed films, the eighth and last CV cycle was used systematically. Indeed, as can be seen on Figure 4a, the first cycle always presented a significantly lower overpotential than the following ones, which can be attributed to the fact that the electrode surface is initially still in the metallic Ni state. It then quickly transforms upon further anodic polarization into a nickel oxide or hydroxide during the following cycles.<sup>8</sup> Indeed, according to Sun et al., the Ni oxidation state at the surface of the electrode is close to +3 because of anodization of Ni in aqueous KOH.<sup>9</sup> This statement was confirmed by Kirov, who showed layers of NiOOH forming on the surface of a Ni electrode at potentials where the OER takes off.<sup>10</sup> Moreover, during charging and discharging, several phase transformations can occur between the different nickel hydroxide variants, as summarized by the Bode cycle in Figure 5. Based on this cycle, one can expect the co-existence of 2 limiting discharged phases ( $\alpha$ - and  $\beta$ -Ni(OH)<sub>2</sub>) and 2 limiting charged phases ( $\gamma$ - and  $\beta$ -NiOOH).<sup>11</sup> It has long been known that  $\alpha$ -Ni(OH)<sub>2</sub> spontaneously ages to  $\beta$ -Ni(OH)<sub>2</sub> in KOH solutions.<sup>12</sup>

Figure 4b shows in more detail the same CV curves at low anodic overpotential, which can be taken as characteristic for further oxidation of Ni oxides into Ni hydroxides. It can be clearly noticed that the oxidation peak shifts to smaller potentials and higher current density during consecutive cycling. The same is being observed for the

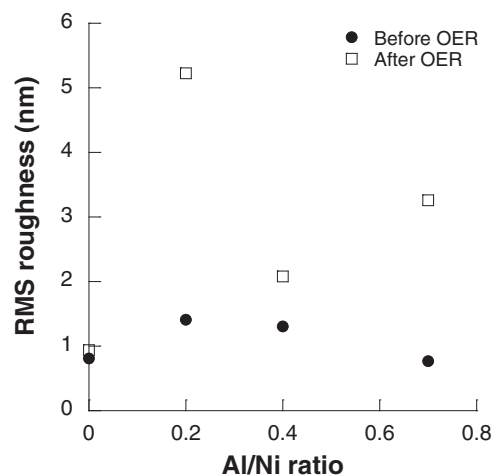


**Figure 3.** RMS roughness before and after electrochemical cycling as a function of Al/Ni ratio.

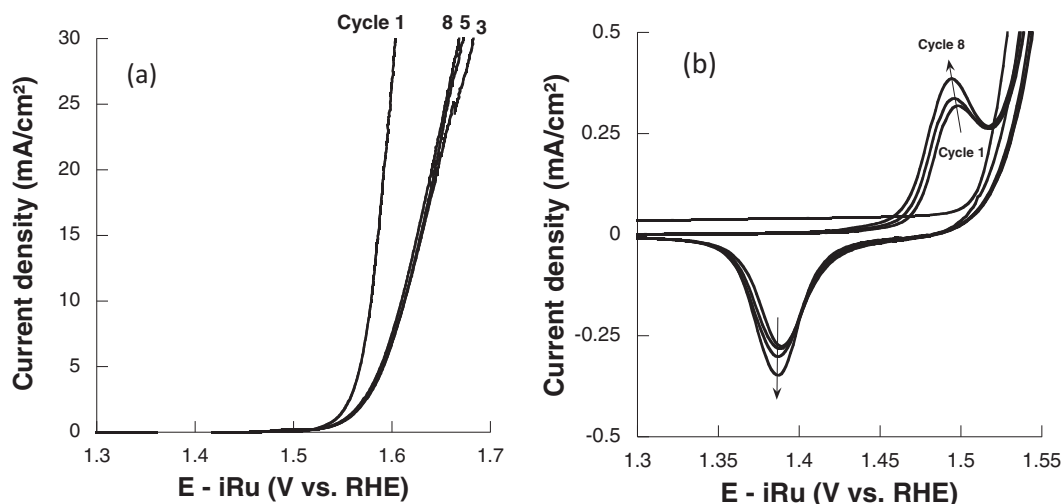


**Figure 4.** (a) Representative comparison of 8 CV cycles for an Al/Ni = 0.7 electrode; (b) Detail of the same CV curves at low anodic overpotential, characteristic for further oxidation of Ni oxides into Ni hydroxides.

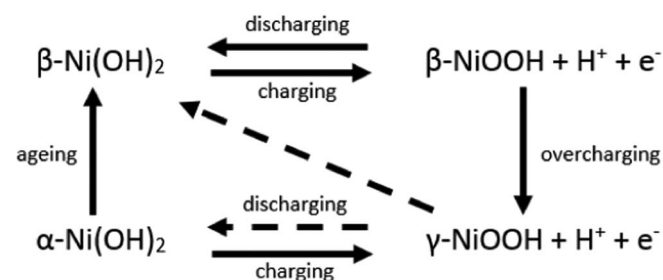
reduction peak. Our observed shift of the anodic peak to lower overpotentials is the opposite of what has been reported in Boettcher et al.<sup>8</sup> In the latter, redox wave shifting was attributed to the presence of Fe impurities, a ppm level contamination being sufficient to cause a peak shifting of about 20–30 mV. In Ref. 8 such Fe impurities were found to result in a shift of the anodic Ni<sup>2+</sup>/Ni<sup>3+</sup> oxidation peak to higher potentials, because the presence of Fe stabilizes the Ni<sup>2+</sup> oxidation state. We believe that our shift of the redox peak to lower potentials during cycling is the result of Al leaching out of our electrode as the Ni-Al gradually de-alloys. At the same time, the anodic peak grows due to the growth of a hydrous Ni layer with cycling. Considering that there is still a significant amount of Al in our electrodes prior to electrochemical cycling, Al can be expected to leach out rather rapidly as we begin cycling, so that by cycle 8 most of the Al will be removed. In any case, the observed (relative) trends reported in the current paper with respect to the different Al/Ni ratio's are not expected to be affected by the anticipated presence of Fe-impurities, since all samples have systematically been subjected to the same grade electrolyte and results have been reported for the 8<sup>th</sup> cycle.

Figure 6 then shows the CV's for all different electrodes, allowing to compare the electrochemical performances of our de-alloyed electrodes to the one for pure Ni. It can be seen that, even though the leaching of the film was not very selective, our Ni(Al) electrodes present a significantly lower overpotential than the pure Ni electrode. Indeed, at 10 mA/cm<sup>2</sup>, which is a commonly used reference value in the OER literature corresponding to the current density for a 10% efficient solar water-splitting device,<sup>15</sup> the OER potential is equal to 1.67, 1.53, 1.62 and 1.54 V for electrodes with initial Al/Ni ratio's equal to 0, 0.2, 0.4, and 0.7, respectively. In other words, for the same current density the energy consumption of the cell decreases, or for the

same potential the current density and hence the O<sub>2</sub> production rate is much larger for the de-alloyed Ni(Al) electrodes. An optimum in terms of overpotential (Figure 7a) and Tafel slope (Figure 7b) is being observed for the Al/Ni = 0.2 electrode: a decrease in overpotential of as much as 140 mV is obtained at 10 mA/cm<sup>2</sup> as compared to the pure Ni electrode, coinciding with a decrease in Tafel slope from 51 to 46 mV/decade. However, from these two graphs, the electrochemical performance does not seem to correlate in a straightforward way with the initial Al/Ni ratio of the electrodes.

A much more convincing correlation can be extracted when combining the electrochemical data of Figure 7 with the morphological ones of Figure 3. Indeed, as shown in Figure 8, both the overpotential at 10 mA/cm<sup>2</sup> (a) and the Tafel slopes (b) tend to decrease monotonically with increasing surface roughness (RMS) measured after the OER. We anticipate at this stage that the increased roughness of the de-alloyed electrode surface favors gas bubble detachment during OER, resulting in the observed and correlated lowering of the overpotential.

In this respect, Lu et al.<sup>18</sup> have studied hierarchically structured, three-dimensional NiFe electrodes deposited onto Ni foams, and



**Figure 5.** Bode cycle for Ni anodes, representing the different transformations that may occur upon charging and discharging.

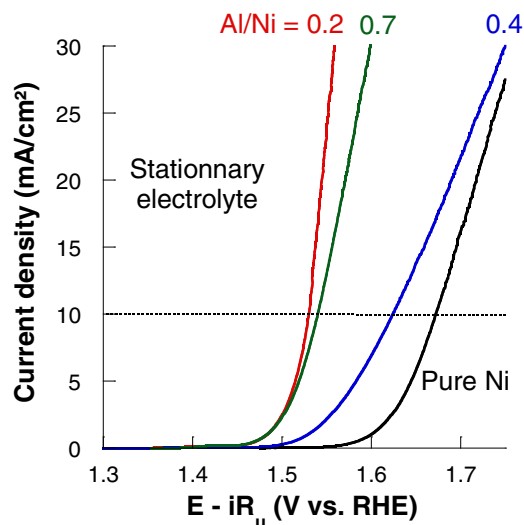


**Figure 6.** Cyclic voltammograms for initial Al/Ni ratios equal to 0 (pure Ni), 0.2, 0.4 and 0.7, taken at 0.01 V/s in a stagnant, O<sub>2</sub> saturated 1 mol/L KOH electrolyte.

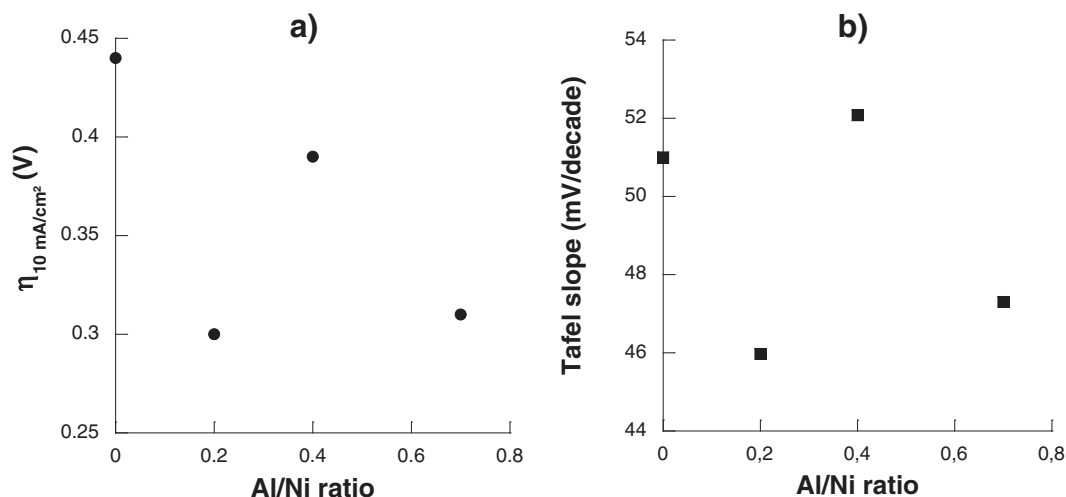


**Figure 7.** (a) Overpotential at 10 mA/cm<sup>2</sup> and (b) Tafel slopes as a function of initial Al/Ni atomic ratio.

pointed out that the current density obtained at an overpotential of 400 mV in a 0.1 mol/L KOH electrolyte was about 3.6 times higher than for planar NiFe electrodes. They attributed this improvement to the macroporous nature of these electrodes, with a roughness factor increase of about 50, which enabled gas bubble detachment in addition to the intrinsically high activity of the NiFe nanosheet catalyst. Furthermore, they also pointed out that the polarization curve for the planar electrodes was significantly affected by gas bubble generation, and exhibited an important drop in OER current. On the other hand, polarization curves obtained with the macroporous NiFe electrodes showed almost no decrease, suggesting a very low impact of gas bubbles on the OER activity. Moller et al.<sup>14</sup> have also studied Al/Ni catalysts leached into NaOH and KNaC<sub>4</sub>H<sub>4</sub>O<sub>6</sub>·4H<sub>2</sub>O, leading to an electrochemical active surface area that was up to 517 times larger than that of a polished nickel electrode. This resulted in a decrease in overpotential of 50 mV at 300 mA/cm<sup>2</sup> compared to polished nickel. Another study that hints to a significant effect of the electrode morphology on its electrochemical performance is the study by Ahn et al.<sup>5</sup> They pointed out that needle-like Ni catalysts both had higher roughness and higher electrochemical activity as compared to flat and smooth Ni catalysts. Indeed, they reported an RMS roughness increase (flat = 12 nm < smooth = 24 nm < cauliflower-like = 41 nm < needle-like = 52 nm) correlating directly to an increased OER

current density taken at 0.9 V during the first CV: flat = 31 mA/cm<sup>2</sup> < smooth = 48 mA/cm<sup>2</sup> < cauliflower-like = 91 mA/cm<sup>2</sup> < needle-like = 96 mA/cm<sup>2</sup>. They also observed a further decrease of the current density during repeated cycling, which they attributed to the blockage of the catalyst surface by bubbles. The ratio of the current decay at 0.9 V was about 70% after the 50<sup>th</sup> cycle for the flat Ni electrode, while it was only 9% for the needle-like Ni electrode. This implies that the bubble effect on the electrochemical performances seemed much less severe with hierarchical morphologies. Even if it is quite difficult to quantitatively compare these literature data to our own results, they all still seem in qualitative agreement with the observation that a decrease in overpotential can be linked directly to an increase in surface roughness of the electrode.

With respect to the Tafel slopes shown in Figs. 8b, our values are also in fair agreement with the ones reported by Lyons et al., who found a Tafel slope of 40 mV/decade for their best Ni electrodes in an oxidizing 1.0 M NaOH electrolyte.<sup>8</sup> Other studies have shown Tafel slopes between 40 and 85 mV/decade, depending on the Ni electrode preparation and the type of alkaline electrolyte.<sup>16,17</sup> Tafel slope values as such are very informative about the dominant reaction mechanism, which for the OER can be either a direct 4 electron transfer:

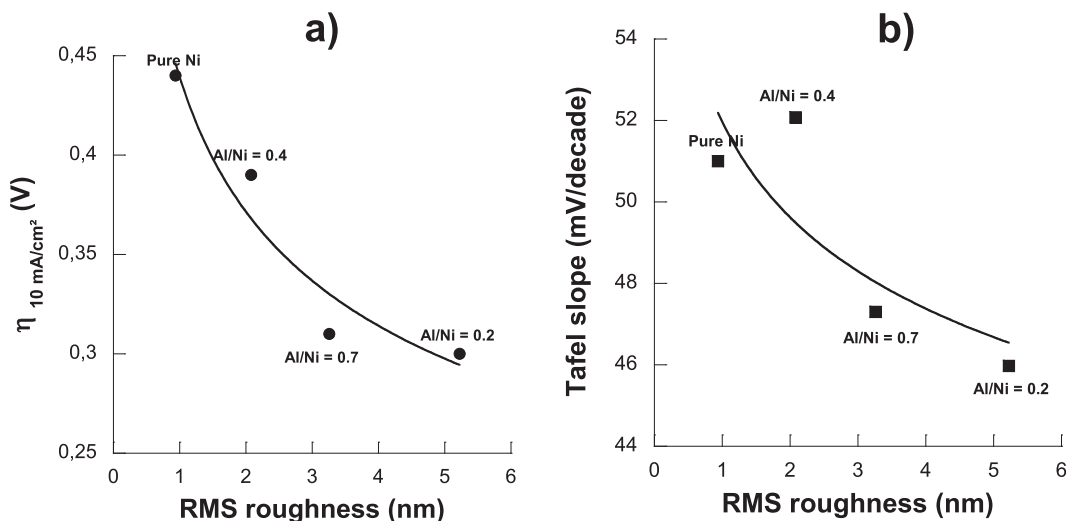
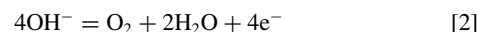
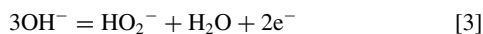


**Figure 8.** (a) Overpotential at 10 mA/cm<sup>2</sup> and (b) Tafel slopes as a function of RMS surface roughness measured after electrochemical cycling.

or an indirect 2 times 2 electron exchange:



Since the Tafel slope can be expressed as

$$\frac{dE}{d(\log j)} = \frac{RT}{(1-\alpha)zF} \quad [5]$$

with  $\alpha$  the charge transfer coefficient (often taken as  $\frac{1}{2}$ ), and  $R$ ,  $T$ ,  $F$  and  $z$  having their usual meaning, its value should be approximately 50 mV/decade for a direct 4 electron exchange mechanism, and only 25 mV/decade for a 2 times 2 electron exchange. Comparing these values with the ones measured by cyclic voltammetry, it can be concluded that the dominant reaction mechanism for our de-alloyed Ni(Al) catalysts is most likely the direct one. Moreover, setting  $z = 4$  in Eq. 5, a more precise average value for the charge transfer coefficient  $\alpha = 0.087 \pm 0.01$  is then obtained for all Ni(Al) electrodes.

Faradaic efficiencies were also calculated for pure Ni and Al/Ni = 0.2 electrodes, in order to verify that no parasite reactions were occurring during OER. They were calculated from the ratio between the experimental and theoretical oxygen production rate. For the first, the volume of oxygen produced at a fixed current density of 10 mA/cm<sup>2</sup> was collected and measured, while the theoretical production rate was calculated from Faraday's law. By this method, faradaic efficiencies at 10 mA/cm<sup>2</sup> were found to be 87.5% and 80.2% for pure Ni and Al/Ni = 0.2 electrodes respectively. The lower efficiency of the Al/Ni = 0.2 electrode in comparison with the pure Ni electrode can be related to the fact that additional Al was also found to be leached out during electrochemical cycling. The contribution of the latter was calculated from its CV to be about 5.5% of the total current, in reasonable agreement with the measured difference in faradaic efficiency between the pure and alloyed Ni electrodes.

Finally, our de-alloyed electrodes also show an excellent short-term stability. Indeed, as shown in Figure 9, the electrode potential remains fairly stable during at least 4 h of chrono-potentiometry at 10 mA/cm<sup>2</sup> in stagnant electrolyte, and this for all the Al/Ni ratios. At this current density, the electrode potential was found to stabilize around 1.65, 1.60, 1.66 and 1.61 V for the Al/Ni = 0, 0.2, 0.4 and 0.7 electrode, respectively.

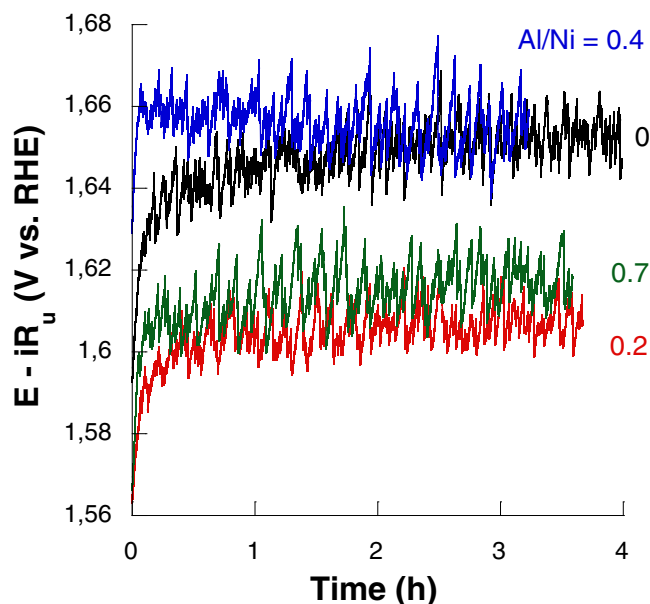


**Figure 9.** Chrono-potentiometry for the different electrodes during 4 hours in stagnant electrolyte at 10 mA/cm<sup>2</sup>.

**Influence of electrolyte flow on OER performance.**—At this stage, it is still an open question to what extent the morphology of our de-alloyed electrodes, more specifically the increased surface roughness, also facilitates the detachment of bubbles at the electrode surface. In this respect, an interesting study was recently published by Mench and Zhang.<sup>19</sup> Their work consisted in developing a transparent and reaction-visible proton exchange membrane electrolyzer cell (PEMEC), coupled with a high-speed and microscale visualization system, in order to observe gas evolving reactions during water splitting. They showed that the reaction sites where oxygen bubbles are generated did not uniformly occupy the catalyst layer (CL), and that these bubbles were preferentially generated at the interface of the CL and liquid/gas diffusion layer (LGDL). Following these observations, they then sputter-coated the thin film catalyst only on the LGDL instead of loading the catalyst on all the membrane using conventional methods. In this way, they pointed out that the electrochemical performance for their new CL were very close to those for a conventional CL, but that the mass activity of the new CL was more than 54 times greater. As a result, it was concluded that the use of expensive catalysts could be significantly reduced in PEMEC while still maintaining the same performance levels.

In order to address the issue of bubble detachment ourselves, the above-reported CV measurements were then repeated under forced electrolyte convection, and results compared with those obtained in stagnant electrolyte. CV data are shown in Figure 10 for, respectively, the pure Ni electrode (a) and the Al/Ni = 0.2 electrode (b). By plotting the potential at 10 mA/cm<sup>2</sup> as a function of electrolyte flow rate, it can be observed in Figure 10c that a forced electrolyte flow through the electrochemical cell strongly influences the OER potential for the pure Ni electrode, but not so much for the de-alloyed electrodes. Indeed, for the pure Ni electrode the potential drop is as much as 40 mV when increasing the electrolyte flow rate from 0 to 0.9 ml/s, while it is a mere 8 mV for the Al/Ni = 0.2 electrode. It can also be concluded from these graphs that the morphological effect on bubble detachment is more important than the effect of electrolyte flow. Indeed, at 10 mA/cm<sup>2</sup>, a potential drop of approximately 70 mV is observed for pure Ni when increasing the flow rate from 0 to 4 ml/s, while a drop of 140 mV appears when going from a pure Ni to an Al/Ni = 0.2 electrode without forced convection.

Further evaluating the results of these CVs with and without forced convection, one can also observe that the Al/Ni = 0.4 electrode presents the weakest, and the Al/Ni = 0.2 electrode the best performance, respectively. This is in agreement with our earlier results shown in Figs. 7 and 8. The fact that the Al/Ni = 0.4 electrode is the least efficient can be attributed to its more pronounced degradation during the leaching step as compared to the other electrodes. Indeed, as seen from the top-view SEM micrographs in Figure 11, circular holes are present on the surface, which may represent the places where bubbles leave the electrode surface taking pieces of catalyst material with them.

## Conclusions

In this work, we have compared the electrochemical performance of different de-alloyed Ni electrodes to the one of untreated, pure Ni. By varying the deposition time and power during the Al-Ni co-deposition, different intermetallic phases (Ni, AlNi<sub>3</sub> and AlNi) have been obtained as shown by XRD. Leaching into concentrated hydroxide solution was carried out in order to obtain de-alloyed thin film electrodes.

Even though very few Al was leached out and intermetallic phases did not change after the leaching step, the electrochemical performance in terms of OER potential was much better for de-alloyed Ni electrodes than for the pure Ni one. Indeed, in the optimal case, the potential at 10 mA/cm<sup>2</sup> was 140 mV lower. This result was attributed to a higher RMS roughness for the de-alloyed electrodes, possibly leading to a better bubble detachment at the electrode surface. The latter was confirmed qualitatively by the fact that forced convection during CV experiments strongly influenced the potential for the pure Ni

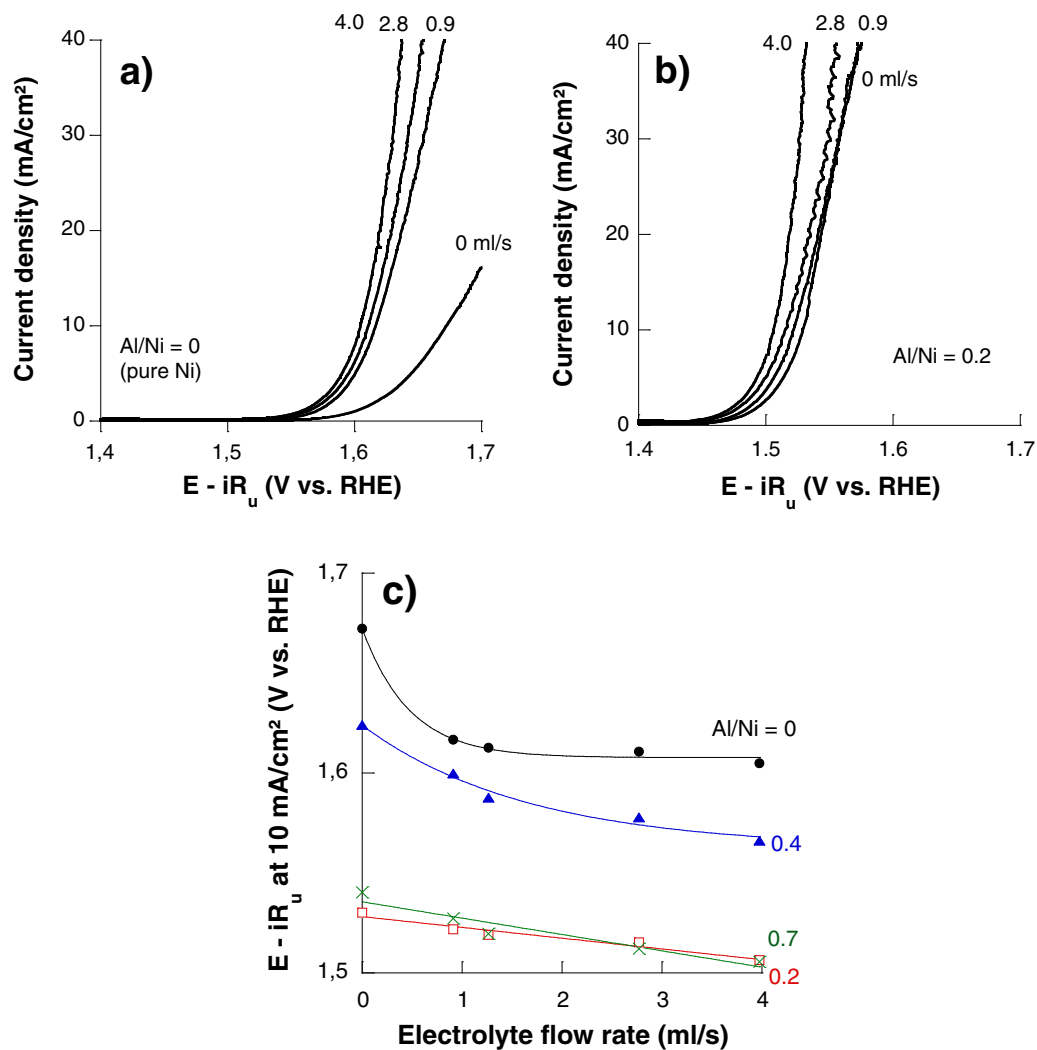


**Figure 10.** Cyclic voltammograms (scan rate 0.01 V/s, O<sub>2</sub> saturated 1 mol/L KOH) at different electrolyte flow rates for (a) pure Ni and (b) an initial Al/Ni ratio equal to 0.2. (c) Effect of electrolyte flow on the OER potential at 10 mA/cm<sup>2</sup> for electrodes with Al/Ni = 0 (●), 0.2 (□), 0.4 (▲) and 0.7 (x).

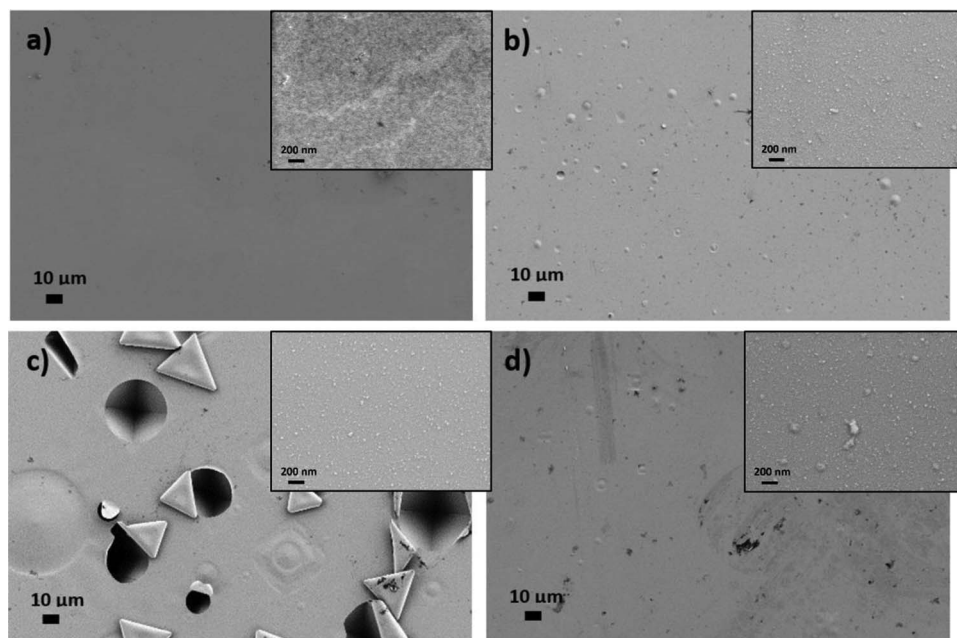


**Figure 11.** Top-view SEM micrographs after leaching of a) pure Ni, b) Al/Ni = 0.2, c) Al/Ni = 0.4 and d) Al/Ni = 0.7.

electrode, but much less for the de-alloyed electrodes. Our de-alloyed Ni thin film electrodes also turned out to be fairly stable in 1 mol/L KOH: the OER potential at 10 mA/cm<sup>2</sup> remained constant for approximately 4 h.

### Acknowledgments

Financial support from the Marie-Curie ITN Project FunMat (EJD 641640) is gratefully acknowledged. We would also like to thank Ronny Santoro for ICP-OES, and Frédéric Van Wonterghem for the XRD measurements.

### References

1. A. R. Zeradjanin, F. La Mantia, J. Masa, and W. Schuhmann, Utilization of the catalyst layer of dimensionally stable anodes – Interplay of morphology and active surface area, *Electrochimica Acta*, **82**, 408 (2012).
2. V. Trieu, B. Schley, H. Natter, J. Kintrup, A. Bulan, and R. Hempelmann, RuO<sub>2</sub>-based anodes with tailored surface morphology for improved chlorine electro-activity, *Electrochimica Acta*, **78**, 188 (2012).
3. R. A. Rincon, E. Ventosa, F. Tietz, J. Masa, S. Seisel, V. Kuznetsov, and W. Schuhmann, Evaluation of perovskites as electrocatalysts for the oxygen evolution reaction, *European Journal of Chemical Physics and Physical Chemistry*, **15**, 2810 (2014).
4. A. R. Zeradjanin, A. A. Topalov, Q. Van Overmeere, S. Cherevko, X. Chen, E. Ventosa, W. Schuhmann, and K. J. J. Mayrhofer, Rational design of the electrode morphology for oxygen evolution – enhancing the performance for catalytic water oxidation, *Royal Society of Chemistry*, **4**, 9579 (2014).
5. S. H. Ann, I. Choi, H.-Y. Park, S. J. Hwang, S. J. Yoo, E. Cho, H. J. Kim, D. Henkensmeier, S. W. Nam, S. K. Kim, and J. H. Jang, Effect of morphology of electrodeposited Ni catalysts on the behavior of bubbles generated during the oxygen evolution reaction in alkaline water electrolysis, *Chemical Communications*, **49**, 9323 (2013).
6. C. McCrory, S. Jung, I. Ferrer, S. Chatman, J. Peters, and T. Jaramillo, Benchmarking hydrogen evolving reaction and oxygen evolving reaction electrocatalysts for solar water splitting devices, *Journal of the American Chemical Society*, **137**, 4347 (2015).
7. L. Celko, L. Klakurkova, and J. Svejcar, Diffusion in AlNi and AlNiCr interfaces at moderate temperatures, *Defect and Diffusion Forum*, **297–301**, 771 (2010).
8. L. Trotochaud, S. L. Young, J. K. Ranney, and S. W. Boettcher, Nickel-iron oxyhydroxide oxygen – evolution electrocatalyst: the role of intentional and incidental iron incorporation, *Journal of the American Chemical Society*, **136**, 6744 (2014).
9. K. Sun, N. Park, Z. Sun, J. Zhou, J. Wang, X. Pang, S. Shen, S. Y. Noh, Y. Jing, S. Jin, P. K. L. Yu, and D. Wang, Nickel oxide functionalized silicon for efficient photo-oxidation of water, *Energy & Environmental Science*, **5**, 7872 (2012).
10. S. Marini, P. Salvi, P. Nelly, R. Pesenti, M. Villa, and Y. Kiros, Oxygen evolution in alkali with gas diffusion, *Hydrogen Energy*, **38**, 11496 (2013).
11. M. Lyons and M. Brandon, A comparative study of the oxygen evolution reaction on oxidized nickel, cobalt and iron electrodes in base, *Journal of Electroanalytical Chemistry*, **641**, 119 (2010).
12. D. S. Hall, D. J. Lockwood, C. Bock, and B. R. MacDougall, Nickel hydroxides and related materials: a review of their structures, synthesis and properties, *Proceedings of the Royal Society A*, **471**, 2174 (2014).
13. L. Trotochaud, S. L. Young, J. K. Ranney, and S. W. Boettcher, Nickel-iron oxyhydroxide oxygen – evolution electrocatalyst: the role of intentional and incidental iron incorporation, *Journal of the American Chemical Society*, **136**, 6744 (2014).
14. C. K. Kjartansdottir, L. P. Nielsen, and P. Moller, Development of durable and efficient electrodes for large-scale alkaline water electrolysis, *International Journal of Hydrogen Energy*, **38**, 8221 (2013).
15. Y. Gorlin and T. F. Jaramillo, A bifunctional nonprecious metal catalyst for oxygen reduction and water oxidation, *Journal of the American Chemical Society*, **132**, 13612 (2010).
16. R. D. L. Smith, M. S. Prévot, R. D. Fagan, S. Trudel, and C. P. Berlinguette, Water oxidation catalysis: electrocatalytic response to metal stoichiometry in amorphous metal oxide films containing iron, cobalt and nickel, *Journal of the American Chemical Society*, **135**, 11580 (2013).
17. D. Chade, L. Berlouis, D. Infield, A. Cruden, P. T. Nielsen, and T. Mathiesen, Evaluation of Raney nickel electrodes prepared by atmospheric plasma spraying for alkaline water electrolyzers, *International Journal of Hydrogen Energy*, **38**, 14380 (2013).
18. X. Lu and C. Zhao, Electrodeposition of hierarchically structured three-dimensional nickel-iron electrodes for efficient oxygen evolution at high current densities, *Nature Communications*, **6**, 6616 (2015).
19. J. Mo, Z. Kang, S. T. Retterer, D. A. Cullen, T. J. Toops, J. B. Green Jr., M. M. Mench, and F.-Y. Zhang, Discovery of true electrochemical reactions for ultrahigh catalyst mass activity in water splitting, *Science Advances*, **2**, e1600690 (2016).